Integrated colloidal deformation to advanced polymer network design through polymer-nanoparticle alternating hybrids

Dongdong Zhou,[1†] Ruikun Sun,[2†] Andrew Wijesekera,[3] Shalin Patil,[2] Zhanhui Gan,[1] Ting Ge,[3] Xue-Hui Dong,[1*] and Shiwang Cheng[2*]*

[1]South China Advanced Institute for Soft Matter Science and Technology, School of Emergent Soft Matter, South China University of Technology, Guangzhou 510640, P. R. China
[2]Department of Chemical Engineering and Materials Science, Michigan State University, East Lansing, MI 48824, United States
[3]Department of Chemistry and Biochemistry, University of South Carolina, Columbia, South Carolina 29208, United States

Abstract

Current polymer network design suffers from intrinsic trade-offs, where polymer networks with high modulus often turn out to be in short of stretchability or fracture toughness. Here, we show a novel polymer network design through polymer-nanoparticle alternating hybrids that enable integrating the *non-polymeric* colloid deformation into polymer network design. The new class of polymer network exhibits colloidal yielding at small deformation before conformational change at higher elongation ratios, enabling *simultaneous* achievement of high Young's modulus of $E \approx 10-50\ MPa$, high yield strength of $\sigma_Y \sim 3-5\ MPa$, large stretchability of $\lambda \sim 7-10$, and high fracture energy density of $\Gamma \sim 30\ MJ/m^3$. These results demonstrate a successful strategy to decouple the molecular mechanics for yield from that for stretchability or toughness, leading to new polymer networks design.

† These authors contribute equally to the work.
* Corresponding Authors. Email: xdong@scut.edu.cn (X.D); tingg@mailbox.sc.edu (T.G); chengsh9@msu.edu (S.C)

1. Introduction

Advanced polymer networks with combined high modulus, large stretchability, and high toughness are desirable for emerging applications in energy, environment, medication, and healthcare.[1-8] However, conventional polymer network design suffers from several intrinsic trade-offs, where polymer networks with high modulus often end up in short of stretchability and toughness.[9, 10] These trade-offs have been primarily attributed to the different dependences of mechanical properties on the molecular weight between crosslink points, M_x, of a polymer network.[11, 12] For instance, the shear modulus of polymer network is inversely proportional to M_x, $G \sim M_x^{-1}$, and the maximum elongation-at-break scales with the square-root of the M_x, $\lambda \sim M_x^{1/2}$. Consequently, polymer networks with larger M_x favor higher elongation-at-break, and *at the same time* suffer from smaller modulus and lower fracture energy density. Thus, elastomers design through adjusting M_x alone is fundamentally limited and cannot simultaneously improve the modulus, the elongation-at-break, yield strength, and toughness.[9, 10, 13]

Various strategies have been proposed to enhance *simultaneously* the modulus, yield strength, and toughness of polymer networks, including double networking,[14-19] introducing dynamics or reversible interactions in polymer networks,[16, 20-24] domain transformation,[25] and embedding fillers.[26-29] Key design rules are to introduce energy dissipation mechanisms and at the same time maintaining network elasticity.[9, 10] Recent studies also show important roles of minimizing the flaw sizes, enabling simultaneously stiffening or fracture of a large amount of polymer chains,[30] and enhancing the near-crack dissipation.[13] However, *none* of these approaches can overcome the aforementioned tradeoffs in the design of polymer network, where entropic changes of network strands still dictate the mechanical responses.[11]

On the other hand, *non-polymeric* materials, such as colloids or granular materials, have been utilized to sustain load with high modulus and large yield strength.[31] The elastic modulus and yield strength of colloidal materials are controlled by their local cage barrier[31, 32] for hopping that is fundamentally different from the polymer elasticity originated from polymer conformational change (entropy).[12] In principle, an integration of the non-polymeric colloid mechanics into the polymer network design could enable decoupling the mechanical mechanisms for yielding and stretchability, and thus provide alternative solutions to address the intrinsic modulus-stretchability trade-off. However, current integration of colloidal interactions to polymer network design through polymer composites design (or polymer nanocomposites) only leads to a mild increment in the modulus and a reduced polymer stretchability.[33, 34] Therefore, a seamless integration of the colloidal deformation modes to the polymer network design has not yet been achieved.

In this work, we integrate colloidal deformation into polymers for advanced polymer network design. Different from previous approaches focusing on controlling M_x, we design novel polymer-nanoparticle alternating hybrids as model systems that can assemble into new supra-macromolecular structured polymer networks. Mechanical measurements show that the new types of polymer hybrids can exhibit *simultaneously* high Young's modulus ($E \approx 10-50\ MPa$), high yield strength ($\sigma_y \sim 3-5\ MPa$), high stretchability (elongation to failure, $\lambda \sim 7-10$), and high fracture energy density ($\Gamma \sim 30\ MJ/m^3$), bypassing the well-known modulus-stretchability trade-offs in advanced polymer network design.

2. Materials and Methods

2.1 Materials.

The following chemicals were used as received: 2-mercaptoethanol (98+%, TCI), 2,2-

dimethoxy-2-phenylacetophenone (DMPA, Irgacure 2959, 99%, Sigma-Aldrich), 1-butanethiol (98+%, Adamas), 4-pentynoic acid (98+%, Adamas), N,N′-diisopropylcarbodiimide (DIC, 98+%, Adamas), 4-dimethylaminopyridine (DMAP, 99+%, Adamas), 1,4-benzenedimethanol (98+%, Adamas), 2-bromo-2-methylpropionyl bromide (98+%, Adamas), triethylamine (99%, Adamas), N, N, N′, N″,N″-pentamethyl diethylenetriamine (PMDETA, 99+%, TCI), tetrahydrofuran (THF, 99.5+%, General-Reagent), dichloromethane (DCM, 99.5+%, General-Reagent), Petroleum Ether (PE, boiling range 60 °C to 90 °C, General-Reagent), Ethyl Acetate (EA, 99.5+%, General-Reagent), Toluene (99%, Guangzhou chemical reagent factory), Methanol (MeOH, General-Reagent, 99.5+%), Ethanol (EtOH, 99.5+%, General-Reagent).

Copper(I) Bromide (CuBr, 99+%, Aladdin) was stirred in acetic acid for 24 h, washed with ethanol and diethyl ether. Styrene (99+%, Adamas) was filtered through silica gel before polymerization. OctaVinyl polyhedral oligomeric silsesquioxane (T8-VPOSS, 98%, Gileader Advanced material) was recrystallized in THF. Anhydrous solvents, including toluene, DCM, THF, were obtained with an INERT Pure Solv System (Inert Corporation, USA).

2.2 Chemical synthesis.

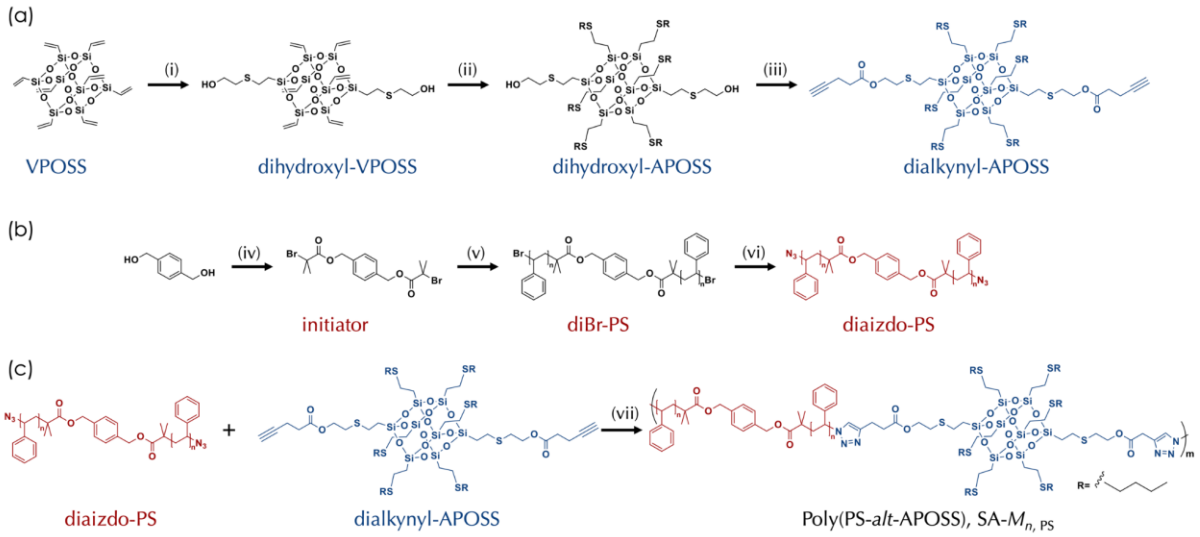

Figure 1. Schemes of the synthesis of (a) dialkynyl-APOSS; (b) diaizdo-PS (b), and (c) Poly(PS-*alt*-APOSS). Reagents and conditions: (i) OctavinylPOSS, 2-mercaptoethanol, DMPA, UV 365 nm; (ii) 1-butanethiol, DMPA, UV 365 nm; (iii) Dihydroxy-APOSS, 4-pentynoic acid, DMAP, DIC; (iv) 1,4-benzenedimethanol, triethylamine, 2-bromo-2-methylpropionyl bromide; (v) Styrene, CuBr, PMDETA; (vi) NaN_3, DMF; (vii) CuBr/PMDETA.

2.2.1 Synthesis of Dialkynyl-APOSS

Synthesis of dihydroxyl-VPOSS. OctavinylPOSS (30.0 g, 47.4 mmol), 2-mercaptoethanol (7.41 g, 94.8 mmol), and DMPA (140 mg, 0.55 mmol) were dissolved in THF (350 mL), and irradiated with UV (365 nm) for 30 min. After removing solvent, the crude product was isolated by silica gel chromatography. A gradient mixture of EA/DCM (v/v from 1/20 to 1/4) was used as eluents to afford the product as white powder. ^{1}H NMR (500 MHz, $CDCl_3$, ppm, δ): 6.15-5.87 (18H, -C*H*=C*H*$_2$), 3.72 (4H, -CH_2C*H*$_2$OH), 2.69-2.65 (8H, -C*H*$_2$C*H*$_2$SC*H*$_2$$CH_2$OH), 1.07 (4H, -SiC*H*$_2$-).

Synthesis of dihydroxyl-APOSS. Dihydroxyl-VPOSS (2.00 g, 2.53 mmol), 1-butanethiol (2.28 g, 25.30 mmol,), and DMPA (41.0 mg, 0.16 mmol) were dissolved in THF (20 mL). After UV irradiation (365 nm) for 30 min, solvent was removed, and the residue was purified by silica gel chromatography with PE/EA (4/1, v/v) as eluent to afford the products (colorless oil liquids). ^{1}H

NMR (500 MHz, $CDCl_3$, ppm, δ): 3.72 (4H, -$CH_2C\underline{H_2}OH$), 2.69-2.65 (8H, -$CH_2C\underline{H_2}SC\underline{H_2}CH_2OH$ and -$CH_2C\underline{H_2}SC\underline{H_2}CH_2CH_2$-), 1.65-1.50 (12H, -$CH_2SCH_2C\underline{H_2}CH_2CH_3$), 1.45-1.35 (12H, -$CH_2SCH_2CH_2C\underline{H_2}CH_3$), 1.08-1.00 (16H, -$SiC\underline{H_2}CH_2OH$ and -$SiC\underline{H_2}CH_2CH_2$-), 0.95-0.89 (18H, -$CH_2CH_2C\underline{H_3}$).

Synthesis of dialkynyl-APOSS. Dihydroxyl-APOSS (2.00 g, 1.50 mmol) and 4-pentynoic acid (0.16 g, 1.65 mmol) were mixed together into a round bottom flask. DMAP (0.18g, 1.5 mmol) were added in a glove box and dissolved in dry DCM (20 mL). DIC (2.0 mL) was then added slowly at 0 °C. The mixture was stirred at room temperature overnight. The reaction was filtered, and the solvent was removed in vacuo. Purification by column chromatography using hexane/ethyl acetate (10/90) as eluent gave the product (1.80g, 90%). ^{1}H NMR (500 MHz, $CDCl_3$, ppm, δ): 3.72 (4H, -$CH_2C\underline{H_2}OH$), 2.75 (4H, -$OCOC\underline{H_2}CH_2CCH$), 2.69-2.45 (36H, -$CH_2C\underline{H_2}SC\underline{H_2}CH_2OH$, -$CH_2C\underline{H_2}SC\underline{H_2}CH_2CH_2$-, and -$OCOCH_2C\underline{H_2}CCH$), 1.98 (2H, -$OCOCH_2CH_2CC\underline{H}$), 1.65-1.50 (12H, -$CH_2SCH_2C\underline{H_2}CH_2CH_3$), 1.45-1.35 (12H, -$CH_2SCH_2CH_2C\underline{H_2}CH_3$), 1.08-1.00 (16H, -$SiC\underline{H_2}CH_2OH$ and -$SiC\underline{H_2}CH_2CH_2$-), 0.95-0.89 (18H, -$CH_2CH_2C\underline{H_3}$).

2.2.2 Synthesis of Diaizdo-Polystyrene (diaizdo-PS)

Synthesis of the bifunctional initiator. 1,4-benzenedimethanol (2.00 g, 14.47 mmol) and triethylamine (5 mL) were dissolved in dry DCM (20 mL) in a round bottom flask. The mixture was stirred at 0 °C, and 2-bromo-2-methylpropionyl bromide (16.63 g, 73.36 mmol) was added slowly. The mixture was stirred at room temperature overnight. The reaction was filtered, and the solvent was removed in vacuo. Purification by column chromatography using hexane/ethyl acetate

(10/90) as eluent gave the product (5.68 g, 90%). ^{1}H NMR (500 MHz, $CDCl_3$, ppm, δ): 7.39 (4H, -OCH_2ArCH_2O-), 5.21 (4H, -OCH_2ArCH_2O-), 1.95 (12H, Br$C(CH_3)_2CO$-).

Synthesis of α,ω-dibromo-polystyrene (diBr-PS). Styrene (12.0 g, 115 mmol), bifunctional initiator (82.86 mg, 0.19 mmol), and CuBr (83 mg, 0.58 mmol) was dissolved in toluene (12 g) in an 100 mL Schlenk flask. After three freeze-pump-thaw cycles, PMDETA (111 mg, 0.58 mmol) was added quickly under a nitrogen atmosphere. The mixture was stirred at 90 °C for 3 h and then quenched in ice-water bath. A short silica gel column was used to remove the copper complex. The collected solution was concentrated and precipitated into methanol. The polymer was collected by filtration as a white solid (2.4 mg, 20 % yield). ^{1}H NMR ($CDCl_3$, 500 MHz, ppm, δ): 7.40-6.30 (139H, -OCH_2ArCH_2O- and -CH(Ar)CH_2-), 5.21 (4H, -OCH2ArCH2O-), 2.60-1.20 (81H, -CH(Ar)CH_2-), 1.95 (12H, Br$C(CH_3)_2CO$-). SEC: M_n = 2.8 kg/mol, PDI = 1.08.

Synthesis of α,ω-diazido-polystyrene (diazido-PS). DiBr-PS (1.00 g, 0.24 mmol) and sodium azide (NaN_3, 0.15 g, 2.38mmol) were dissolved in 10 mL of DMF in a 50 mL flask. After stirred for 24 h, the mixture was poured into 100 mL of CH_2Cl_2 and then was washed by water (100 mL × 3). After being dried by anhydrous Na_2SO_4, the organic layer was concentrated followed by precipitation into methanol. The product was collected by filtration as a white solid (0.88 g, 88%). ^{1}H NMR ($CDCl_3$, 500 MHz, ppm, δ): 7.40-6.30 (139H, -OCH_2ArCH_2O- and -CH(Ar)CH_2-), 5.21 (4H, -OCH2ArCH2O-), 2.60-1.20 (81H, -CH(Ar)CH_2-), 1.95 (12H, Br$C(CH_3)_2CO$-). SEC: M_n = 2.8 kg/mol, PDI = 1.08; M_n = 4.2 kg/mol, PDI = 1.09.

2.2.3 Synthesis of Poly(PS-alt-APOSS)

Synthesis of althernating polymer Poly(PS-*alt*-APOSS). Diaizdo-PS (250.0 mg, 0.60 mmol), dialkynyl-APOSS (79.2 mg, 0.60 mmol), and CuBr (83 mg, 0.58 mmol) in toluene (5.0 mL) was added into a 50 mL Schlenk flask. After degassed by three freeze-pump-thaw cycles, PMDETA (220 mg, 1.16 mmol) was added quickly under a nitrogen atmosphere. The reaction mixture was stirred at 90 °C for 3 h and then quenched in ice-water bath. A short silica gel column was used to remove the copper complex. The collected solution was concentrated and precipitated into methanol. The polymer was collected by filtration as a white solid (260 mg, 78 % yield). NMR of Poly(PS-*alt*-APOSS) is presented in **Figure S3b**. In the following discussions we abbreviate Poly(PS-*alt*-APOSS) as SA and highlight the molecular weight of PS block in the hybrid. For example, SA-2.8k refers to the Poly(PS-*alt*-APOSS) hybrids with PS molecular weight of 2.8 kg/mol (number average). We have also synthesized diaizdo terminated linear PS2.9k and a copolymer between diaizdo terminated PS2.9k and the dialkynyl terminated molecular linkers, 1,4-phenylenebis(methylene) bis(pent-4-ynoate), for alternating polymer with molecular weight of 16.3k (alt-PA-16.3k) as references. SEC: SA-2.8k with PS block molecular weight of 2.8 kg/mol, M_n=29.8 kg/mol, PDI = 2.01; SA-4.2k with PS block molecular weight of 4.2 kg/mol, M_n = 29.7 kg/mol, PDI = 2.03.

2.3 Methods.

Automated column chromatography was conducted on a SepaBean^{TM} machine T (SanTai Technologies, China) with an automated variable wavelength UV-VIS detector (200-400 nm).

^{1}H-NMR spectra were recorded on Bruker 400 MHz spectrometers using $CDCl_3$ (Cambridge) as deuterated solvent. The spectra were referenced to the residual proton impurities in the $CDCl_3$ at

d 7.26 ppm.

Size exclusion chromatography (SEC) analyses were conducted on a Tosoh HLC-8320 instrument equipped with three TSKgel columns (SuperH2000, SuperH3000, and SuperH4000) in series, a double flow type RI detector, and a UV-8320 UV detector, under an eluent flow rate of 0.6 mL/min (THF). Regular SEC calibrations were conducted with polystyrene standards (Polymer Laboratories).

Small angle x-ray scattering (SAXS) measurements were conducted on thin-film like SA hybrids with a thickness of 0.3 mm at the beamline 12-ID-B at Advanced Photon Source at Argonne National Laboratory with an x-ray energy of 13.3 keV. The exposure time is 0.5 s. The scattered x-ray intensities were measured using a 2-D Pilatus 2M detector with a sample to detector distance of 2.1 m (covering a scattering wavevector of Q = 0.003 $Å^{-1}$ to 0.9 $Å^{-1}$). Before measurements, we calibrated the absolute intensity using glassy carbon and the Q values of detector pixels using silver behenate. The 2-D isotropic scattering images were converted to 1-D intensity curves, $I(Q)\ vs\ Q$, through azimuthally average after solid angle correction and then normalizing with the intensity of the transmitted x-ray beam flux, using the beamline software.

Differential scanning calorimetry (DSC) was performed to characterize the glass transition temperature, T_g, of the SA hybrids and the dialkyne functionalized APOSS nanoparticles. The T_g were determined at the inflection point of the specific heat capacity step upon heating at a heating rate of 10 K/min. The T_g of linear PS2.9k and Alt-PS-16.3k were determined upon heating at a heating rate of 5 K/min. To suppress the influence of the crystallization of dialkynyl functionalized

APOSS, a fast quenching (~ 100 K/min) is employed to prepare the amorphous dialkyne functionalized APOSS.

Linear rheology and mechanical measurements were performed on an Anton Paar MCR 302 rotational rheometer equipped with a CTD600 oven. The temperature accuracy of this oven is $\pm 0.1\ K$. Linear viscoelastic spectra of the neat polystyrene with number average molecular weight of 22 kg/mol (PS22k) and polydispersity index of 1.05, SA-2.8k, and SA-4.2k hybrids were collected through small amplitude oscillatory shear (SAOS) on a pair of aluminum parallel plates of 8 mm in diameter with a measuring gap of 1 mm. A wide temperature range is involved in the measurements that covers temperatures close their T_g (shear modulus ~ 10^9 Pa) as well as high temperatures to access the terminal modes (such as PS22k) or shear modulus ~ 10^2-10^3 Pa (for SA-2.8k and SA-4.2k). The strain amplitude was set to 0.1% at temperatures close T_g and 3 % when the shear modulus fall below 10^6 Pa. The liner viscoelastic spectra of PS22k, SA-2.8K, and SA-4.2k were constructed through the time-temperature superposition principle.

Uniaxial extension tests of SA-2.8k and SA-4.2k at constant Hencky Strain rates from 0.003 s^{-1} to 6 s^{-1} on a third generation of Sentmanat Extensional Rheometer fixture (SER-3) that mounted onto the Anton Paar MCR302. The polymer hybrids, SA-2.8k or SA-4.2k, were first press molded into thin films of 0.3 mm in thickness that were cut into rectangular strips of 3 mm in width and 15 mm in length before testing. The testing temperatures are at $T = 333\ K$ and $353\ K$ for SA-2.8k and SA-4.2k respectively.

2.4 Computer simulations.

Coarse-grained molecular dynamics (CGMD) simulations have been performed to understand the assembly and the mechanical properties of the SA-2.8k hybrid. A recently estabilished mapping to PS is used in the determination of system parameters.[35] For atactic PS, a coarse-grained bead of mass m is mapped to 297.19 g/mol, which leads to 9.4 coarse-grained beads in a PS block with 2.8 kg/mol. The number of beads per segment is rounded off to 10. Each bead is of size σ, which is mapped to 0.76 nm for atactic PS (**Figure 2a**). Any two pairs of beads may interact via the truncated and shifted Lennard-Jones (LJ) potential with interaction strength ε and cut-off distance $r_c = 1.12\,\sigma$, which corresponds to purely repulsive interactions between the beads. The unit time for the LJ potential is $\tau = \sigma\sqrt{m/\varepsilon}$. Neighboring beads in the segment are connected by the finitely extensible nonlinear elastic (FENE) potential with an equilibrium bond length of $0.96\,\sigma$. A bond-bending potential in the form $U_{bend}(\theta) = k_{bend}\,(1 + \cos\theta)$ is used to couple adjacent bonds with bond angle θ. The bending stiffness $k_{bend} = 0.944\,\varepsilon$ allows each Kuhn monomer to contain 2.44 coarse-grained (CG) beads. This results in a Kuhn length $l_K = 2.35\,\sigma$, which is mapped to 1.79 nm.

The nanoparticle is modeled as a smooth sphere of diameter $d = 2\,\sigma$, which is mapped to 1 nm, approximately the size of an APOSS particle. The mass density of the nanoparticle is $\rho_m^{POSS} = 1.9\,m/\sigma^3$, which is 1.9 times larger than PS mass density $\rho_m^{PS} = 1.0\,m/\sigma^3$. The interaction between a polymer bead and a nanoparticle and that between two nanoparticles are both modeled using the colloidal force fields developed by Everaers and Ejtehadi.[36] The polymer-particle interaction is purely repulsive with cut-off distance $r_c = 1.9\,\sigma$. The corresponding Hamaker constant is $A = 75\,\varepsilon$ that corresponds to the athermal condition at $T = 1.0\,\varepsilon/k_B$. The particle-particle interaction is attractive with cut-off distance $r_c = 5.0\,\sigma$. The corresponding Hamaker

constant is $A = 710.784\,\varepsilon$, which may be mapped to a strong strength of $18\,k_B$T on the monomeric length scale σ.

The simulations include 1000 SA-2.8k chains in a simulation box (**Figure 2b**). A constant pressure P is necessary to turn the multiple chains into a dense sample. A Nos*é* – Hoover barostat with $P = 5.1\ \varepsilon/\sigma^3$ and a characteristic damping time $100\,\tau$ was applied to the simulation box together with a Nos*é* – Hoover thermostat with $T = 1.0\,\varepsilon/k_B$ and a characteristic damping time $10\,\tau$. The time step for integrating the equations of motion was $0.001\,\tau$. After $100{,}000\tau$, the resulting equilibrium box dimensions are $L_x = L_y = L_z = 54.9\,\sigma$, and the mass density $\rho_m^{hybrid} = 1.28\,m/\sigma^3$. The mechanical deformation on the dense melt of hybrid chains was performed in the uniaxial tensile loading mode. The box size in the z-direction was increased at a constant engineering strain rate $10^{-3}\tau^{-1}$ and $10^{-4}\tau^{-1}$. The rates allowed the tensile test to be completed within a feasible simulation time window, while also allowing the PS strand of 10 CG beads, whose relaxation time is about $10^3\tau$, to rearrange itself during the test. The box sizes in the x- and y-directions varied at constant pressure components $P_x = P_y = 5.1\,\varepsilon/\sigma^3$, which were maintained using the Nos*é* – Hoover barostat with a characteristic damping time $100\,\tau$. During the uniaxial tensile test, a Nos*é* – Hoover thermostat with $T = 1.0\,\varepsilon/k_B$ and a characteristic damping time $10\,\tau$ was applied to maintain the melt temperature. All simulations were peformed using the LAMMPS package.[37]

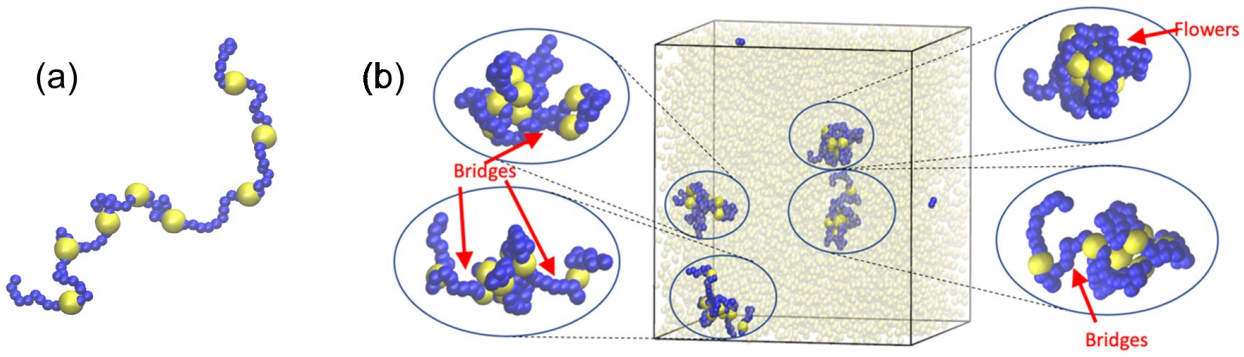

Figure 2 (a) A representative SA-2.8k chain in the simulation that is composed of 9 PS strands and eight APOSS particles connecting alternatively. (b) A snapshot of the simulation composing of 1000 SA-2.8k chains under equilibrium, where chain conformation and assembly structures can be analyzed.

3. Results and Discussions.

Two model polymer hybrids, SA-2.8k and SA-4.2k with similar total molecular weight of ~29 kg/mol, have been synthesized to test the hypothesis of integrating colloidal interaction into the polymer network. Small-angle x-ray scattering (SAXS) has been employed to characterize the structure of these hybrids. **Figure 3a** presents the scattering intensity, $I(Q)$, of the SA-2.8k and SA-4.2k after background scattering subtraction, where Q is the scattering wavevector. Two distinct peaks are well-resolved at high and intermediate Q, offering characterizations of the distribution of APOSS. The peaks at $Q_{pp} \approx 0.54\ \text{Å}^{-1}$ and $Q_{pp} \approx 0.59\ \text{Å}^{-1}$ represent the characteristic distances of d_{pp}~1.2 nm and d_{pp}~1.1 nm between APOSS particles in SA-2.8k and SA-4.2k, respectively. Due to the dense packing of the APOSS within the clusters, d_{pp} provides quantifications of the diameter of APOSS. The scattering peaks at $Q_{cc} \approx 0.20\ \text{Å}^{-1}$ (for SA-2.8k) and $Q_{cc} \approx 0.16\ \text{Å}^{-1}$ (for SA-4.2k) are due to the scattering of APOSS clusters, implying the formation of supramolecular structures in these hybrids. The characteristic distances of the APOSS clusters are thus d_{cc}~3.14 nm for SA-2.8k and d_{cc}~3.9 nm for SA-4.2k. The volume

fraction of APOSS is 34% in former and 26% in latter. Assuming all APOSS particles are in the clusters, there are ~6 APOSS nanoparticles in one cluster for SA-2.8k and ~12 APOSS in one cluster for SA-4.2k. Since each SA-2.8k chain has ~7 APOSS particle and each SA-4.2k chain has ~5 APOSS particle. The average sizes of ~ 6 APOSS/cluster for SA-2.8k and the average sizes of ~12 APOSS/cluster for SA-4.2k implies a *minimum* of $\sim 1/7 \sim 14\%$ of PS strands of SA-2.8k and $2/12 \sim 17\%$ of SA-4.2k serving as polymer bridges. However, the exact number density of bridges requires detailed information of the conformation SA hybrids. The inter-cluster surface-to-surface distances are $d_{ICS} \approx 1.0\, nm$ for SA-2.8k and $d_{ICS} \approx 1.4\, nm$ for SA-4.2k. Note that the end-to-end distance of PS with a molecular weight of 2.8 and 4.2 kg/mol are $R_{ee} \sim 3.5\, nm$ and $R_{ee} \sim 4.3\, nm$ respectively, both of which are significantly larger than the d_{ICS} of the corresponding SA hybrids. The SAXS measurements thus imply a formation of PS loops at the corona of APOSS clusters and a leading intra-molecular associating of SA hybrids (inset of **Figure 3a**).

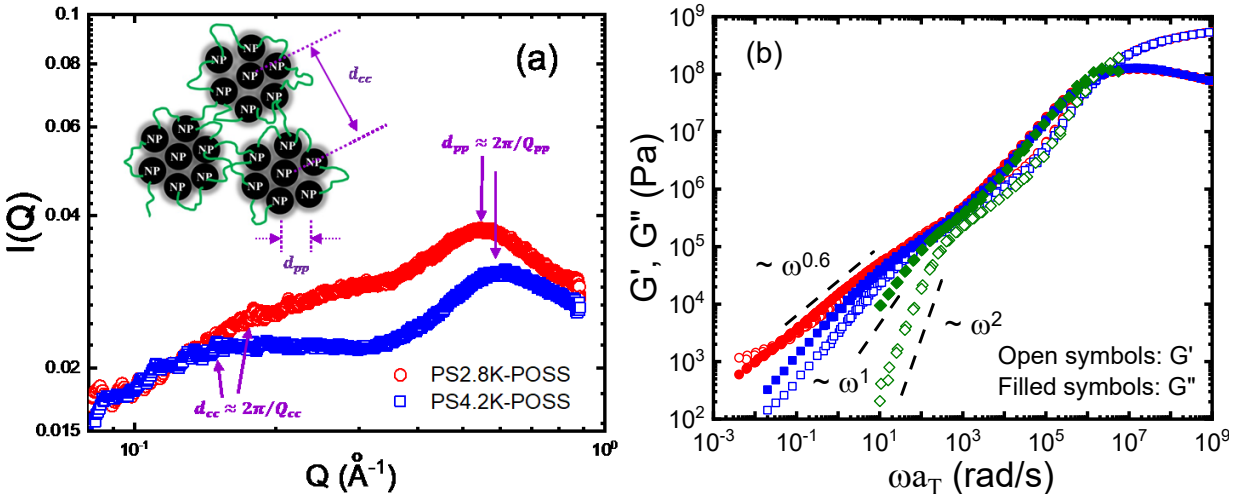

Figure 3 (a) Small angle x-ray scattering of SA-2.8k and SA-4.2k. The inset cartoon presents a sketch of the clustering and cluster organization in SA hybrids. **(b)** Linear viscoelastic master curves of SA-2.8k (red circles), SA-4.2k (blue squares), and their comparison with the neat PS22K (olive diamonds). All the master curves were constructed at a reference temperature of $T_{ref} = 393\, K$. The spectra of SA-2.8k was shifted 0.32 time horizontally and the spectra of PS22k was shifted 6,000 times horizontally to match the glassy region of the SA-4.2k as shown in the panel. (b). The large deviation between SA hybrids and the neat

PS22K at the low frequency and the emergence of low-frequency modulus plateau of SA-2.8k indicate the network formation of the hybrids.

To confirm the network formation, we turn to linear viscoelastic measurements. As shown in **Figure 3b**, both the linear viscoelastic master curves of SA-2.8k and SA-4.2k have strong deviations from that of the PS22k, especially in the low frequency region. The linear viscoelastic spectra of PS22k, SA-2.8k, and SA-4.2k were constructed through the time-temperature superposition principle. The dynamics shift factors, a_T, were presented in **Figure S5** and no vertical shifts was applied for all the master curves. Although a large reduction in glass temperature, T_g, of SA hybrids have been observed compared with PS22k (**Figure S6**), only slight differences have been found at the Rouse dynamics region between the SA and the linear PS, suggesting small modifications to the sub-chain motions of SA hybrids. One possibility for the low T_g of SA hybrids is the influence of APOSS particles that has $T_g \approx 248\ K$ (**Figure 6a**). To understand large drop in T_g of the SA hybrids compared with the neat PS of similar molecular weight, we further synthesized diaizdo terminated linear PS2.9k and the Alt-PS-16.3k from the copolymerization of the diaizdo terminated PS and dialkynyl terminated molecular linker, 1,4-phenylenebis(methylene) bis(pent-4-ynoate). The Alt-PS-16.3k shows a much higher T_g than the PS2.9k (**Figure S6c**), supporting the low T_g of SA hybrids originating from the low T_g of APOSS. Unlike the linear PS22k, a weak modulus plateau at $G_N{\sim}10^5\ Pa$ emerges for both SAs at the intermediate frequency region, confirming the network formation of SA. The network formation might be due to the PS bridges connecting APOSS clusters. According to rubber elasticity theory, $G_N \approx \nu k_B T$ with ν being the number of network strands per unit volume, k_B the Boltzmann constant, and $T = 318\ K$ the testing temperature. This leads to $\nu \approx 2.28\ \times 10^{25}\ m^{-3}$ that is only a small fraction ($\sim 16 - 22\%$) of the total number density of PS strands of $\nu_{PS} \approx 1.4 \times 10^{26}\ m^{-3}$

for SA-2.8k and $\nu_{PS} \approx 1.05 \times 10^{26}\ m^{-3}$ for SA-4.2k. The $\sim 16 - 22\%$ of PS bridging strands is only slightly higher than $\sim 14\% - 17\%$ of PS bridging of SA hybrids estimated from the SAXS measurements, which is consistent with the primary loop formation during the assembly of SA hybrids. On the other hand, if intermolecular associating is the major clustering mechanism, a rubbery plateau of $G \approx \rho RT/M_x \sim 9 \times 10^5\ Pa$ and $\sim 4.6 \times 10^5\ Pa$ should be anticipated for SA-2.8k and SA-4.2k, with $\rho \sim 1.0\ g/cm^3$, $R = 8.314\ J/(mol * K)$, and $T = 318\ K$. These values are much higher than the experimental observations of $G_N \sim 10^5\ Pa$ for SAs. Therefore, the linear viscoelastic measurements confirm the intramolecular associating as the leading associative mechanism of APOSS in SA hybrids, supporting the SAXS measurements. We would like to emphasize that attaching small nanoparticles, such as POSS, into polymer chain has been actively studied before. However, most previous works focus on side-chain attachment that favor intra-molecular association.[38] As a result, qualitative different structures and linear viscoelastic properties have been observed from the ones presented in the current work,[39] highlighting an interesting role of nanoparticles incorporating into the backbone of hybrids. Synthetically, incorporating POSS particles in the chain backbone have also been pursued with limited success,[38, 40-45] and no previous works seek for the applications of polymer-POSS hybrids on advanced elastomers.

At the low frequency region, clear signatures of gel formation are present with $G' \sim G'' \sim \omega^{0.6}$ and a low-frequency plateau, $G_{lp} \sim 10^3\ Pa$, for SA-2.8k. A similar observation has been found for SA-4.2k with the G' and G'' approaching each other at the lowest testing frequencies. The low-frequency plateau thus indicates network formation at much larger length scales originated from the elasticity of the supra-macromolecular network strands. Before diving into the details of mechanical responses of the SAs, we would like to comment on the low elastic

modulus G_{lp}~$10^3\ Pa$ of these hybrids that are comparable to that of super-soft biological tissues.[46-48] We notice there is currently *only one* other type of *solvent-free* super-soft elastomers based on bottle-brush polymers that can access elastic modulus as low as $10^3\ Pa$.[49] The obtained low elastic modulus of SA can thus serve as an alternative way for future preparation of *solvent-free* super-soft elastomers.

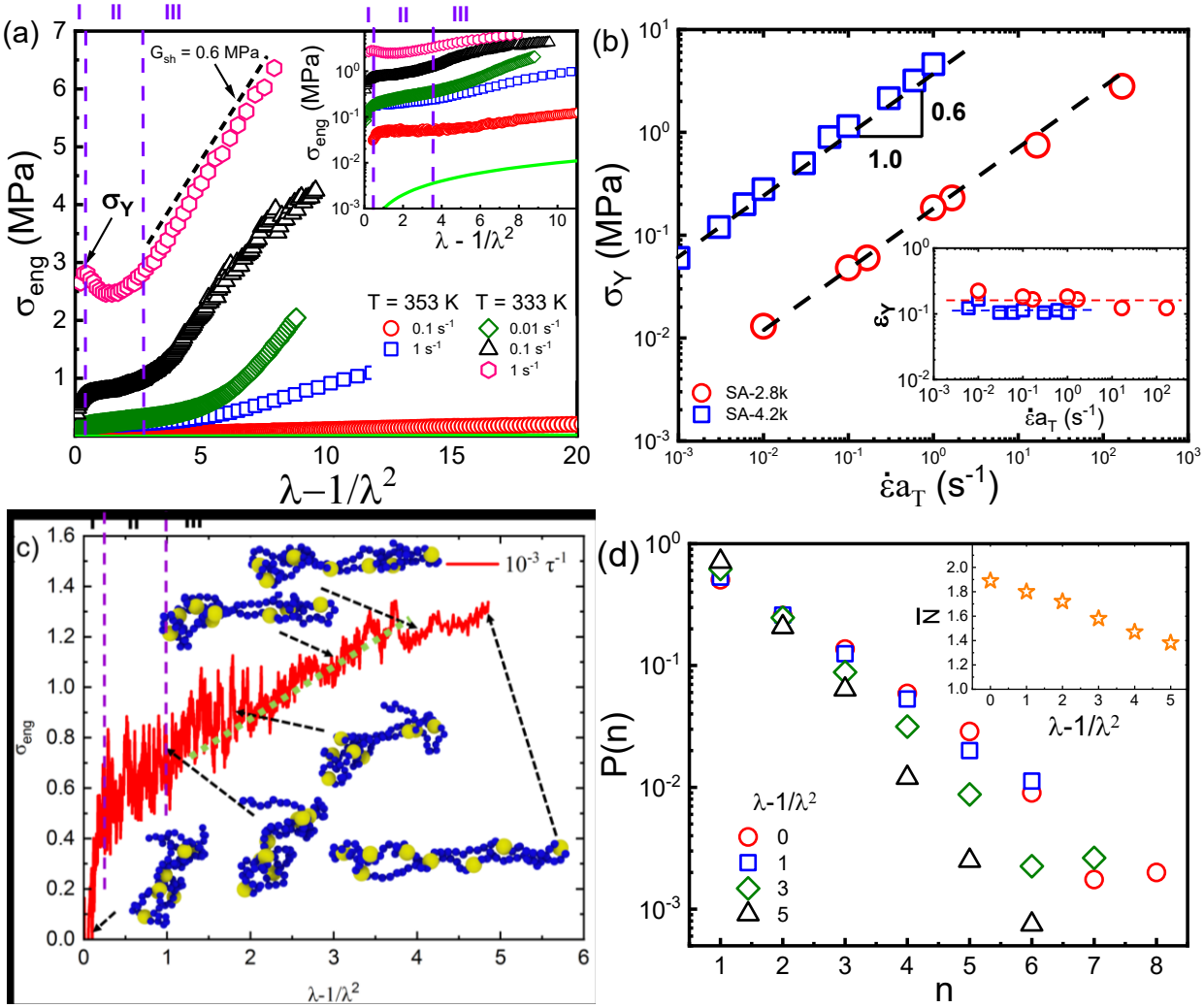

Figure 4 (a) Engineering stress, σ_{eng}, vs $\lambda - 1/\lambda^2$ of SA-2.8k at T = 333 K and T = 353 K, where λ is the elongation ratio. The inset is the same data in the semi-log representation, where the solid green line is the prediction of neo-Hookean relationship. **(b)** The scaling behaviors of yield stress, σ_Y, and yield strain, ε_Y, with the effective deformation rates, $\dot{\varepsilon}a_T$, where $\dot{\varepsilon}$ is the Hencky Sstrain rate and a_T is the shift factor. The reference temperature of SA-2.8k is $T_{ref} = 353\ K$ and that of SA-4.2k is $T_{ref} = 348\ K$. (c) σ_{eng} vs $\lambda - \lambda^{-2}$ of SA-2.8k from the simulations at the indicated strain rate. The inset presents the structural evolution

of the polymer hybrid with deformation. (d) Probability $P(n)$ of an APOSS particle in an intramolecular cluster that consists of n particles. The inset shows the average cluster size as a function of $\lambda - \lambda^{-2}$.

How do the SA hybrids respond to large deformation? **Figure 4a** presents the uniaxial extension of SA-2.8k (open symbols) at constant Hencky strain rate, $\dot{\varepsilon} = d(\ln \lambda)/dt$ with λ being the elongation ratio, and their comparison with the prediction of neo-Hookean law (solid green lines), $\sigma_{eng} = G(\lambda - 1/\lambda^2)$ where σ_{eng} is the engineering stress, and $G \approx 10^3\ Pa$ is the elastic modulus of the network. The experimental testing temperature is at $T = 333\ K$, which is well-above the glass transition temperature of SA-2.8k, $T_g = 293\ K$. The deformation of SA-2.8k can be divided into three Regions with (i) an initial sharp rise in the stress at $\lambda < 1.2$ (Region I), (ii) a yield point around $\lambda \sim 1.2$ ($\varepsilon \sim 0.2$) followed by a very weak tensile stress increase upto $\lambda \sim 4 - 5$ (Region II). No signs of necking or necking propagation were observed in Region II. (iii) a sharp strain hardening (Region III) at $\lambda > 5$ before rupture. The end of the region II and the onset of region III depend strongly on the deformation rates.

Region I covers the initial mechanical response with Young's modulus and yield strength, both of which show strong strain rate dependence. In contrast, the strain rate has a much less influence on the stress rise in Regions II and III. These features can be better presented through the σ_{eng} vs $\lambda - 1/\lambda^2$ (**Figure 4a**). The inset of **Figure 4a** provides the amplified stress vs deformation curve at the initial stage of the deformation. The Young's modulus, E, the yield stress, σ_Y, the yield strain, $\varepsilon_Y = ln\lambda_Y$ with λ_Y being the elongation ratio at the yield point, and the strain hardening modulus, G_{sh}, can be obtained from the mechanical characterizations. Interestingly, the Young's modulus of SA-2.8k is ~30 MPa at $\dot{\varepsilon} = 1\ s^{-1}$ and $T = 333\ K$ that reduces to 0.6 MPa at $\dot{\varepsilon} = 0.01\ s^{-1}$ that is much stronger than the amplitude of the complex modulus of SA-2.8k at the same deformation rates (**Figure S7**), highlighting a non-network origin of the deformation.

Quantitative analyses also reveal interesting scaling behaviors between σ_Y, ε_Y, and $\dot{\varepsilon}$, with $\sigma_Y \sim \dot{\varepsilon}^{0.6}$ and $\varepsilon_Y \sim \dot{\varepsilon}^0$ (**Figure 4b**), which are different from that of the entangled polymers exhibiting $\sigma_Y \sim \dot{\varepsilon}^{0.33}$ and $\varepsilon_Y \sim \dot{\varepsilon}^{0.33}$.[50-54] Recent studies showed similar scaling behavior of true stress $\sigma_t \sim \dot{\varepsilon}^{0.5}$ at the true stress maximum and the corresponding yield strain $\varepsilon_H \sim \dot{\varepsilon}^0$ for deformation of associative network during the sol-to-gel transition.[55] This observation is interesting. However, we see several differences between the observed yielding of the SA hybrids and that of the associative network: (i) The current study is focus on the engineering stress instead of true stress with $\sigma_t = \lambda\sigma_{eng}$; (ii) The yield strain ε_H of associative network correlates well with the deformation of network strands, $\varepsilon_H \sim \ln(\sqrt{M/M_k})$ with M and M_k being the molecular weight of the strand and the molecular weight of the Kuhn segment of polymer. $M_k = 850\ g/mol$ is found for PS.[56] As a result, $\varepsilon_Y \sim \ln\left(\sqrt{2800/850}\right) = 0.60$ for SA-2.8k and $\ln\left(\sqrt{4200/850}\right) = 0.80$ for SA-4.2k should be anticipated, both of which are much larger than the observed values of $\varepsilon_Y \sim 0.1 - 0.2$. In addition, if the yielding mechanism is due to the deformation of the PS strands, one should also anticipate a higher yield strain of SA-4.2k than SA-2.8k, which has not been observed. Therefore, the yielding of the SA hybrids is unlikely due to the deformation of PS strands between the APOSS particles. On the other hand, the observed scaling behaviors of $\sigma_Y \sim \dot{\varepsilon}^{0.6}$ and $\varepsilon_Y \sim \dot{\varepsilon}^0 \sim 0.1 - 0.2$ of SA remind of the yielding response of colloidal or soft glassy materials,[57, 58] implying a success incorporation of colloidal deformation into the network design.

Beyond the yielding, σ_{eng} changes little at the entire Region II. An instantaneous modulus, $G_a \equiv \partial\sigma_{eng}/\partial(\lambda - \lambda^{-2}) \sim 10^3\ Pa$, has been identified that is coincidence with the low-frequency plateau from the linear viscoelastic measurements. These analyses point to that the conformational rearrangements of the APOSS clusters regulate the mechanical properties of Region II. Further deformation beyond Region II leads to a strong strain hardening in Region III. Interestingly, the

instantaneous modulus at this region is G_{sh}~0.6 MPa that changes little with deformation rates beyond certain threshold. The very weak strain rate dependence of G_{sh} at high deformation rate is also fundamentally different from that of entangled polymers or elastomers due to the non-Gaussian stretching.[12, 51, 59] Moreover, our hysteresis deformation tests (**Figure S8**) demonstrate an exceedingly low recovery (less than 10%) of the SA hybrids after deformation in the strain-hardening region (Region III), in sharp contrast to the strong elastic response of the strain hardening region of entangled polymers or crosslinked elastomers.[12] Moreover, the $G_{sh} \approx$ 0.6 MPa is found for both the SA-2.8k and the SA-4.2k (**Figure S9**) regardless of the molecular weight of the PS blocks, indicating the APOSS-APOSS interaction rather than the molecular weight of the PS strands dictating the strain hardening of SA hybrids. Combining all these analyses, one can conclude the dissociation of the APOSS from the APOSS clusters as the molecular origin of the high strain hardening in Region III.

To confirm the supra-macromolecular network formation and their deformation mechanism, we have further performed molecular dynamics (MD) simulations. SA-2.8k were mapped into 9 PS blocks connecting alternatingly with 8 APOSS particles. **Figure 2b** provides a snapshot of the simulation at equilibrium, where one can analyze in detail the loops, bridges, and the association of the APOSS. Specifically, we calculate the number fraction $P(n)$ of a APOSS particle belonging to a cluster consisting of n particles. Two APOSS particles from the same hybrid chain are counted in the same intramolecular cluster when the distance between them is smaller than $r_c = 3.0\ \sigma$. This criterion is used because $r_c = 3.0\ \sigma$ is the location of the potential energy minimum for the nanoparticle-nanoparticle interaction. These MD simulations can also help understand their deformation mechanism. **Figure 4c** presents the σ_{eng} vs $\lambda - 1/\lambda^2$ of the SA-2.8k at two deformation rates $10^{-3}\tau^{-1}$. The applied rate was sufficiently slow to allow the

relaxation of a PS strand between two particles, whose relaxation time is $\sim 10^3\ \tau$. The mechanical response can be clearly divided into three distinct regions: (i) the initial sharp rise in stress at small λ along with a clear yield point (**Region I**), (ii) a post-yield region with slight stress rise before strain hardening (**Region II**), and (iii) a strong strain hardening region with a near constant strain hardening modulus (**Region III**). All these features agree well with the experimental observation. Note that experimentally we have a much more pronounced **Region II** due to the much smaller strain rates than the simulation.

Tracking the structures of the supra-macromolecular structures upon deformation show the following interesting features. Before deformation at $\lambda - 1/\lambda^2 = 0$ (**Figure 4d**), $P(n = 1) \approx 50\%$, which means roughly half the particles are not in close contact with any particles from the same chain and thus may contribute to the bridging between different clusters, which is significantly higher than the PS blocks serving as bridges in experiments. Moreover, the population of clusters reduces strongly with an increment in the cluster sizes with the largest clusters containing ~7-8 APOSS particles. The average cluster size, $\bar{N} = \sum nP(n)$, is around 1.9 that is much smaller than the experimental determination of 6. This difference between the simulations and experiments is possibly due to the different kinetic pathways to form the supra-macromolecular structures. Deformation leads to large changes in the sizes and sizes distribution of the clusters (**Figure 4d**): **(i)** The nanoparticle clustering structure remains almost unchanged at the beginning of the deformation from $\lambda = 1$ ($\lambda - 1/\lambda^2 = 0$) to $\lambda = 1.46$ ($\lambda - 1/\lambda^2 = 1$), which covers the initial stress rise (**Region I**) and the post-yield region before strain hardening (**Region II**). **(ii)** Further deformation at $\lambda - 1/\lambda^2 > 2$ leads to strong strain hardening (**Region III**) in mechanical response and a reduction of the population of the large clusters and an increment in the population of small clusters, especially the isolated nanoparticles. **(iii)** The average sizes of the

nanoparticle clusters (inset of **Figure 4d**) reduce progressively upon deformation, which is consistent with the general deformation-induced destruction mechanism of the nanoparticle clusters at large deformation. These observations support the activated cage hopping of the nanoparticle clusters as the leading deformation mechanism at the initial deformation of the hybrid. They also point to the nanoparticle-nanoparticle dissociation as the leading mechanism for strain hardening of the hybrid, which is fundamentally different from the strain hardening of conventional elastomers.

Combining experiments and computer simulations, we propose the following deformation mechanism of SA hybrids: The polymer-POSS hybrid can assemble into supra-macromolecular clusters (the core-shell structure of **Figure 5a).** These supramolecular clusters are loosely connected to form a physical network (the blue solid lines in **Figure 5b**) due to a small fraction of polymer bridges. This hierarchical structure provides the unique mechanical properties. Specifically, the initial deformation involves mainly the rearrangement of the supra-macromolecular clusters (**Figures 5b-Figure 5c**), which can be viewed as a deformation-induced conformational change of the physical network (the blue lines). Importantly, the rearrangement of these core-shell supra-macromolecular clusters is achieved through deformation-induced hopping, in analogous to the yielding of densely packed colloids. This is consistent with the colloidal deformation characteristics of SA hybrids at small strains (Region I). Deformation beyond the yield point is mostly plastic flow of the core-shell supra-macromolecular structures (Region II). The plastic deformation through rearrangement of supra-macromolecular clusters ends when the supra-macromolecular network strands reaches its deformation limit (**Figure 5c**). Beyond this point, further deformation leads to a forced dissociation of supra-macromolecular clusters, giving rise to the strain hardening before failure (**Figure 5d**) (Region III). Since APOSS-APOSS

interactions does not change with varying the molecular weights of the PS strands, this also explains the almost identical strain hardening modulus of SA-2.8k and SA-4.2k.

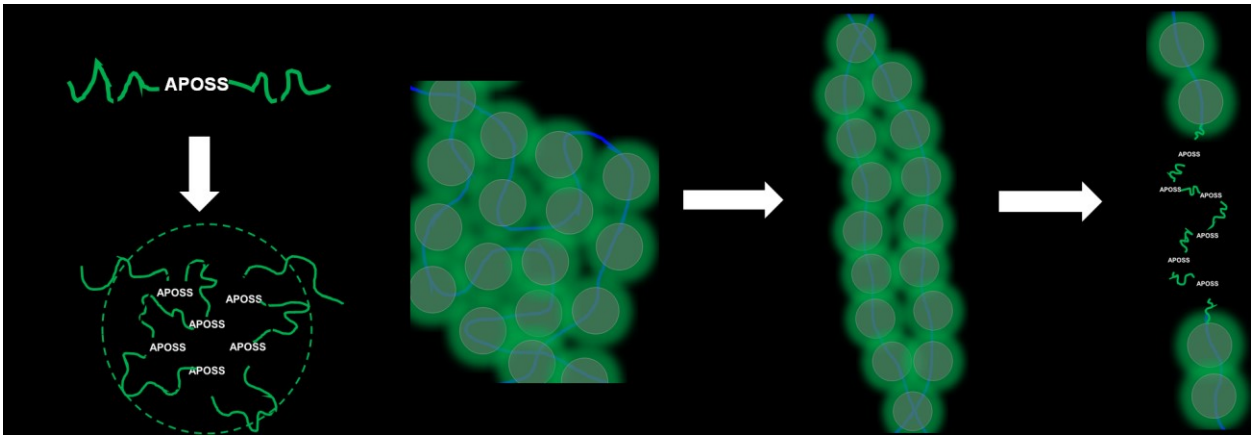

Figure 5. Deformation mechanism of SA hybrids. (a) A sketch of the SA hybrids and its assembly into core-shell structures with APOSS clustering and PS loops as shell. (b). Packing of the core-shell structures in the space and the formation of supra-macromolecular network (the blue lines) due to the small fractions of PS bridges. (c) Rearrangement of the supra-macromolecular network upon deformation. (d) Deformation-induced dissociation of the supra-macromolecule clusters leading to strain hardening of SA hybrids.

The above experiments and simulations demonstrate the SA hybrids exhibit hierarchical structures and multi-scale deformation that are qualitative different from conventional elastomers. Specifically, the colloidal-like deformation at small strains and the subsequent deformation of the supra-macromolecular structures enables simultaneously high yield strength, σ_Y, high elongation-at-break, λ_m. To be more quantitative, we estimate the high fracture energy density, $\Gamma = \int_1^{\lambda_m} \sigma_{eng} d\lambda$, of SA. Experimentally, σ_{eng} and λ_m are direct outcomes of experiments with λ_m being the elongation ratio at the failure. We adopt the classical rubber elasticity theory to compute the theoretical fracture energy density of elastomers by assuming $\sigma_{eng} = G(\lambda - \lambda^{-2})$ and $\lambda_m = \sqrt{N_x}$ being the finite extensibility limit of a network strand with N_x Kuhn monomers.[9-11, 23] $G = \frac{\rho RT}{N_x M_0}$ with $M_0 \approx 850\ g/mol$ being the average molecular weight of a Kuhn monomer of PS.[12]

Varying the N_x leads to a theoretical upper bound of the fracture energy density. **Figures 6a and 6b** present the Young's modulus, E, vs λ_m and Γ vs E of SA, where $E = 2(1+\nu)G$ and $\nu = 0.5$ for rubbery materials.[12] The dashed black lines are the corresponding predictions of the rubber elasticity theory that represents an upper bound for the performance of elastomers. The SA outperforms all other types of polymer networks or elastomers of similar E with a combination of high yield strength, high stretchability, and high fracture energy density. Therefore, the results show that an effective way of overcoming the intrinsic trade-offs in mechanical properties through integrating the colloidal deformation into polymer network design.

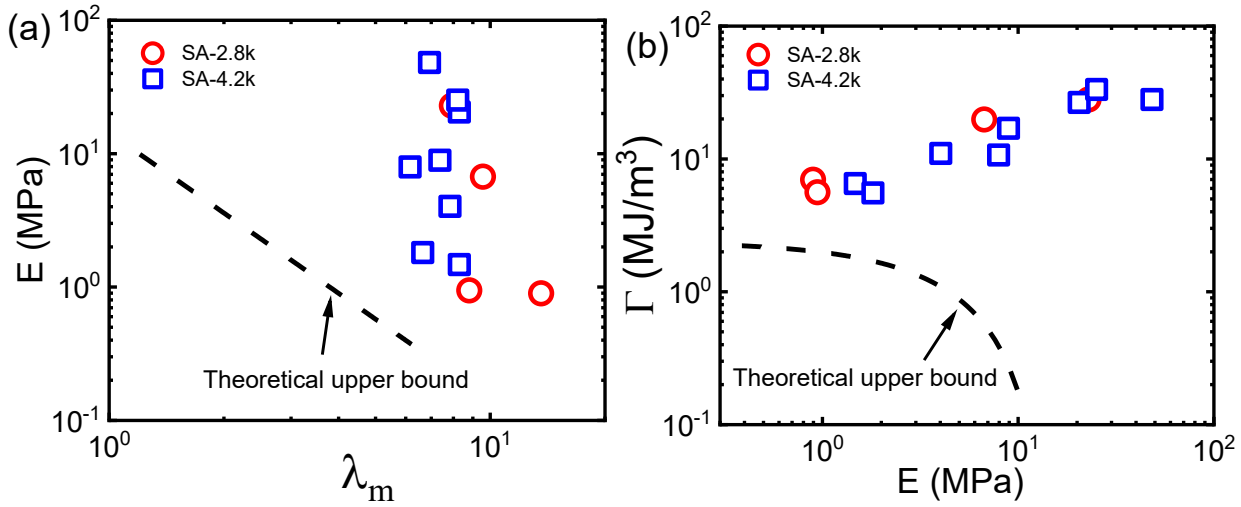

Figure 6 (a) The Young's modulus E vs elongation-at-break λ_m of the polymer hybrid network (the symbols) and their comparison with theoretical predictions from rubber elasticity theory (the dashed line). **(b)**The fracture energy density, Γ, vs E of the polymer hybrid network and their comparison with theoretical predictions from rubber elasticity theory (the dashed line).

4. Conclusions

In conclusion, we have demonstrated a new polymer network design with sequence-controlled alternating polymer-small nanoparticle hybrids to surpass the intrinsic trade-offs of mechanical properties in polymer networks design. Specifically, the strong intramolecular association of small-size nanoparticles, APOSS, in the polystyrene backbone induces interconnected "flower-like" supramolecular structures. The novel hierarchical network structures

can thus integrate seamlessly different deformation mechanisms, including colloidal yielding at small deformation and deformation-induced dissociation of nanoparticles clusters at large strain. As a result, polymer networks with high Young's modulus of $E \sim 30\ MPa$, high yield strength of $\sigma_Y \sim 3\ MPa$, and a high toughness with fracture energy of Γ as high as 30 MJ/m^3 are obtained. These results demonstrate the success of seamlessly synergizing the *non-polymeric* colloidal deformation modes into polymer network, opening new avenues for high-performance elastomers design. Since the nanoparticle-nanoparticle interactions play a crucial role in the assembly and the supra-macromolecular structures formation of the hybrids, we anticipate the nanoparticle sizes and nanoparticle compositions (such as the substitute groups) to play essential roles for the mechanical properties and other macroscopic properties of polymer hybrids. Our future studies will focus on these directions.

Acknowledgement

S.C. acknowledges the support of National Science Foundation with the Award Number NSF-DMR 2211573 for this work. The SAXS measurements were performed at Beamline 12-ID-B of Advanced Photon Source, a U.S. Department of Energy (DOE) Office of Science User Facility operated for the DOE Office of Science by Argonne National Laboratory under Contract No. DE-AC0206CH11357. We thank Dr. Xiaobing Zuo for his help on the SAXS measurements. T. G. thanks the start-up funds from University of South Carolina for supporting the simulations in this work. Computational resources were provided by University of South Carolina flagship computing cluster Hyperion.

Reference

1. D. DeRossi, K. Kajiwara, Y. Osada and A. Yamauchi, eds., *Polymer Gels: Fundamentals and Biomedical Applications*, Springer New York, New York, 1991.
2. S. Bauer, S. Bauer-Gogonea, I. Graz, M. Kaltenbrunner, C. Keplinger and R. Schwödiauer, 25th Anniversary Article: A Soft Future: From Robots and Sensor Skin to Energy Harvesters, *Adv. Mater.* , 2014, **26**, 149-162.
3. N. A. Peppas, J. Z. Hilt, A. Khademhosseini and R. Langer, Hydrogels in Biology and Medicine: From Molecular Principles to Bionanotechnology, *Adv. Mater.* , 2006, **18**, 1345-1360.
4. K. Y. Lee and D. J. Mooney, Hydrogels for Tissue Engineering, *Chem. Rev.* , 2001, **101**, 1869-1880.
5. R. Yoshida, Design of Functional Polymer Gels and Their Application to Biomimetic Materials, *Curr. Org. Chem.* , 2005, **9**, 1617-1641.
6. W. Wang, W. Lu, A. Goodwin, H. Wang, P. Yin, N.-G. Kang, K. Hong and J. W. Mays, Recent advances in thermoplastic elastomers from living polymerizations: Macromolecular architectures and supramolecular chemistry, *Prog. Polym. Sci.* , 2019, **95**, 1-31.
7. W. Balasooriya, C. Clute, B. Schrittesser and G. Pinter, A Review on Applicability, Limitations, and Improvements of Polymeric Materials in High-Pressure Hydrogen Gas Atmospheres, *Polym. Rev.* , 2022, **62**, 175-209.
8. E. Rostami-Tapeh-Esmaeil, A. Vahidifar, E. Esmizadeh and D. Rodrigue, Chemistry, Processing, Properties, and Applications of Rubber Foams, *Polymers*, 2021, **13**, 1565.
9. X. Zhao, Designing toughness and strength for soft materials, *Proc. Nat. Acad. Sci. U.S.A.*, 2017, **114**, 8138-8140.
10. X. Zhao, Multi-scale multi-mechanism design of tough hydrogels: building dissipation into stretchy networks, *Soft Matter*, 2014, **10**, 672-687.
11. G. J. Lake and A. G. Thomas, The strength of highly elastic materials, *Proc. R. Soc. London, Ser. A*, 1967, **300**, 108-119.
12. L. R. G. Treloar, *The Physics of Rubber Elasticity*, Clarendon Press, Oxford, 3rd edn., 2005.
13. S. Lin, C. D. Londono, D. Zheng and X. Zhao, An extreme toughening mechanism for soft materials, *Soft Matter*, 2022, **18**, 5742-5749.
14. J. P. Gong, Why are double network hydrogels so tough?, *Soft Matter*, 2010, **6**, 2583-2590.
15. J. P. Gong, Y. Katsuyama, T. Kurokawa and Y. Osada, Double-Network Hydrogels with Extremely High Mechanical Strength, *Adv. Mater.* , 2003, **15**, 1155-1158.
16. W. Yang, H. Furukawa and J. P. Gong, Highly Extensible Double-Network Gels with Self-Assembling Anisotropic Structure, *Adv. Mater.* , 2008, **20**, 4499-4503.
17. T. C. Suekama, J. Hu, T. Kurokawa, J. P. Gong and S. H. Gehrke, Double-Network Strategy Improves Fracture Properties of Chondroitin Sulfate Networks, *ACS Macro Letters*, 2013, **2**, 137-140.
18. E. Ducrot, Y. Chen, M. Bulters, R. P. Sijbesma and C. Creton, Toughening Elastomers with Sacrificial Bonds and Watching Them Break, *Science*, 2014, **344**, 186-189.
19. Z. Wang, X. Zheng, T. Ouchi, T. B. Kouznetsova, H. K. Beech, S. Av-Ron, T. Matsuda, B. H. Bowser, S. Wang, J. A. Johnson, J. A. Kalow, B. D. Olsen, J. P. Gong, M. Rubinstein and S. L. Craig, Toughening hydrogels through force-triggered chemical reactions that lengthen polymer strands, *Science*, 2021, **374**, 193-196.

20. H. Zhang, Y. Wu, J. Yang, D. Wang, P. Yu, C. T. Lai, A.-C. Shi, J. Wang, S. Cui, J. Xiang, N. Zhao and J. Xu, Superstretchable Dynamic Polymer Networks, *Adv. Mater.* , 2019, **31**, 1904029.
21. J.-Y. Sun, X. Zhao, W. R. K. Illeperuma, O. Chaudhuri, K. H. Oh, D. J. Mooney, J. J. Vlassak and Z. Suo, Highly stretchable and tough hydrogels, *Nature*, 2012, **489**, 133-136.
22. L. Tang, W. Liu and G. Liu, High-Strength Hydrogels with Integrated Functions of H-bonding and Thermoresponsive Surface-Mediated Reverse Transfection and Cell Detachment, *Adv. Mater.* , 2010, **22**, 2652-2656.
23. Z. Zhang, J. Luo, S. Zhao, S. Ge, J.-M. Y. Carrillo, J. K. Keum, C. Do, S. Cheng, Y. Wang, A. P. Sokolov and P.-F. Cao, Surpassing the stiffness-extensibility trade-off of elastomers via mastering the hydrogen-bonding clusters, *Matter*, 2022, **5**, 237-252.
24. P.-F. Cao, B. Li, T. Hong, J. Townsend, Z. Qiang, K. Xing, K. D. Vogiatzis, Y. Wang, J. W. Mays, A. P. Sokolov and T. Saito, Superstretchable, Self-Healing Polymeric Elastomers with Tunable Properties, *Adv. Funct. Mater.* , 2018, **28**, 1800741.
25. A. E. X. Brown, R. I. Litvinov, D. E. Discher, P. K. Purohit and J. W. Weisel, Multiscale Mechanics of Fibrin Polymer: Gel Stretching with Protein Unfolding and Loss of Water, *Science*, 2009, **325**, 741-744.
26. K. Haraguchi and T. Takehisa, Nanocomposite Hydrogels: A Unique Organic–Inorganic Network Structure with Extraordinary Mechanical, Optical, and Swelling/De-swelling Properties, *Adv. Mater.* , 2002, **14**, 1120-1124.
27. Q. Wang, J. L. Mynar, M. Yoshida, E. Lee, M. Lee, K. Okuro, K. Kinbara and T. Aida, High-water-content mouldable hydrogels by mixing clay and a dendritic molecular binder, *Nature*, 2010, **463**, 339-343.
28. T. Huang, H. G. Xu, K. X. Jiao, L. P. Zhu, H. R. Brown and H. L. Wang, A Novel Hydrogel with High Mechanical Strength: A Macromolecular Microsphere Composite Hydrogel, *Adv. Mater.* , 2007, **19**, 1622-1626.
29. F. T. Moutos, L. E. Freed and F. Guilak, A biomimetic three-dimensional woven composite scaffold for functional tissue engineering of cartilage, *Nat. Mater.* , 2007, **6**, 162-167.
30. Y. Wu, D. U. Shah, C. Liu, Z. Yu, J. Liu, X. Ren, M. J. Rowland, C. Abell, M. H. Ramage and O. A. Scherman, Bioinspired supramolecular fibers drawn from a multiphase self-assembled hydrogel, *Proc. Nat. Acad. Sci. U.S.A.*, 2017, **114**, 8163-8168.
31. P. G. de Gennes, Granular matter: a tentative view, *Rev. Mod. Phys.* , 1999, **71**, S374-S382.
32. M. E. Cates, J. P. Wittmer, J. P. Bouchaud and P. Claudin, Jamming, Force Chains, and Fragile Matter, *Phys. Rev. Lett.* , 1998, **81**, 1841-1844.
33. T. A. Vilgis, G. Heinrich and M. Klüppel, *Reinforcement of Polymer Nano-Composites: Theory, Experiments and Applications*, Cambridge University Press, Cambridge, 2009.
34. J. E. Mark, B. Erman and C. M. Roland, *The Science and Technology of Rubber*, Academic Press, 4th edn., 2013.
35. R. Everaers, H. A. Karimi-Varzaneh, F. Fleck, N. Hojdis and C. Svaneborg, Kremer–Grest Models for Commodity Polymer Melts: Linking Theory, Experiment, and Simulation at the Kuhn Scale, *Macromolecules*, 2020, **53**, 1901-1916.
36. R. Everaers and M. R. Ejtehadi, Interaction potentials for soft and hard ellipsoids, *Phys. Rev. E*, 2003, **67**, 041710.
37. A. P. Thompson, H. M. Aktulga, R. Berger, D. S. Bolintineanu, W. M. Brown, P. S. Crozier, P. J. in 't Veld, A. Kohlmeyer, S. G. Moore, T. D. Nguyen, R. Shan, M. J. Stevens, J. Tranchida, C. Trott and S. J. Plimpton, LAMMPS - a flexible simulation tool for particle-

based materials modeling at the atomic, meso, and continuum scales, *Comput. Phys. Commun.* , 2022, **271**, 108171.
38. S.-W. Kuo and F.-C. Chang, POSS related polymer nanocomposites, *Prog. Polym. Sci.* , 2011, **36**, 1649-1696.
39. E. T. Kopesky, T. S. Haddad, R. E. Cohen and G. H. McKinley, Thermomechanical Properties of Poly(methyl methacrylate)s Containing Tethered and Untethered Polyhedral Oligomeric Silsesquioxanes, *Macromolecules*, 2004, **37**, 8992-9004.
40. K. Wei, L. Wang and S. Zheng, Organic–inorganic copolymers with double-decker silsesquioxane in the main chains by polymerization via click chemistry, *J. Polym. Sci., Part A: Polym. Chem.* , 2013, **51**, 4221-4232.
41. K. Wei, L. Wang and S. Zheng, Organic–inorganic polyurethanes with 3,13-dihydroxypropyloctaphenyl double-decker silsesquioxane chain extender, *Polym. Chem.* , 2013, **4**, 1491-1501.
42. N. Liu, L. Li, L. Wang and S. Zheng, Organic-inorganic polybenzoxazine copolymers with double decker silsesquioxanes in the main chains: Synthesis and thermally activated ring-opening polymerization behavior, *Polymer*, 2017, **109**, 254-265.
43. N. Katsuta, M. Yoshimatsu, K. Komori, T. Natsuaki, K. Suwa, K. Sakai, T. Matsuo, T. Ohba, S. Uemura, S. Watanabe and M. Kunitake, Necklace-shaped dimethylsiloxane polymers bearing polyhedral oligomeric silsesquioxane cages with alternating length chains, *Polymer*, 2017, **127**, 8-14.
44. R. Sodkhomkhum and V. Ervithayasuporn, Synthesis of poly(siloxane/double-decker silsesquioxane) via dehydrocarbonative condensation reaction and its functionalization, *Polymer*, 2016, **86**, 113-119.
45. M. A. Hoque, Y. Kakihana, S. Shinke and Y. Kawakami, Polysiloxanes with Periodically Distributed Isomeric Double-Decker Silsesquioxane in the Main Chain, *Macromolecules*, 2009, **42**, 3309-3315.
46. M. Vatankhah-Varnosfaderani, W. F. M. Daniel, M. H. Everhart, A. A. Pandya, H. Liang, K. Matyjaszewski, A. V. Dobrynin and S. S. Sheiko, Mimicking biological stress–strain behaviour with synthetic elastomers, *Nature*, 2017, **549**, 497.
47. S. S. Sheiko and A. V. Dobrynin, Architectural Code for Rubber Elasticity: From Supersoft to Superfirm Materials, *Macromolecules*, 2019, **52**, 7531-7546.
48. S. S. Sheiko, M. H. Everhart, A. V. Dobrynin and M. Vatankhah-Varnosfaderani, Encoding tissue mechanics in silicone, *Science Robotics*, 2018, **3**, eaat7175.
49. W. F. M. Daniel, J. Burdynska, M. Vatankhah-Varnoosfaderani, K. Matyjaszewski, J. Paturej, M. Rubinstein, A. V. Dobrynin and S. S. Sheiko, Solvent-free, supersoft and superelastic bottlebrush melts and networks, *Nat. Mater.* , 2016, **15**, 183-189.
50. S. Q. Wang, S. Ravindranath, Y. Wang and P. Boukany, New theoretical considerations in polymer rheology: Elastic breakdown of chain entanglement network, *J. Chem. Phys.* , 2007, **127**, 064903.
51. Y. Wang, S. Cheng and S. Q. Wang, Basic characteristics of uniaxial extension rheology: Comparing monodisperse and bidisperse polymer melts, *J. Rheol.* , 2011, **55**, 1247-1270.
52. Y. Wang, P. Boukany, S. Q. Wang and X. Wang, Elastic Breakup in Uniaxial Extension of Entangled Polymer Melts, *Phys. Rev. Lett.* , 2007, **99**, 237801.
53. R. Sun, M. Melton, X. Zuo and S. Cheng, Nonmonotonic Strain Rate Dependence on the Strain Hardening of Polymer Nanocomposites, *ACS Macro Letters*, 2020, **9**, 1224-1229.

54. Z. Xu, R. Sun, W. Lu, S. Patil, J. Mays, K. S. Schweizer and S. Cheng, Nature of Steady-State Fast Flow in Entangled Polymer Melts: Chain Stretching, Shear Thinning, and Viscosity Scaling, *Macromolecules*, 2022, **55**, 10737-10750.
55. X. Cao, L. Peng, X. Huang and Q. Chen, A trade-off between hardness and stretchability of associative networks during the sol-to-gel transition, *J. Rheol.* , 2023, **67**, 1119-1128.
56. T. Inoue and K. Osaki, Role of Polymer Chain Flexibility on the Viscoelasticity of Amorphous Polymers around the Glass Transition Zone, *Macromolecules*, 1996, **29**, 1595-1599.
57. P. Sollich, Rheological constitutive equation for a model of soft glassy materials, *Phys. Rev. E*, 1998, **58**, 738-759.
58. P. Sollich, F. Lequeux, P. Hébraud and M. E. Cates, Rheology of Soft Glassy Materials, *Phys. Rev. Lett.* , 1997, **78**, 2020-2023.
59. Y. Wang and S. Q. Wang, Rupture in rapid uniaxial extension of linear entangled melts, *Rheol. Acta* 2010, **49**, 1179-1185.